machines

MDPI

Article

A Decoupling Module Based on a Geometrical-Balance Mechanism for Mitigating Cable Length Variation in Cable-Driven Applications

Van Pho Nguyen [1,2], Sunil Bohra Dhyan [1,2] and Wai Tuck Chow [1,*]

[1] School of Mechanical and Aerospace Engineering, Nanyang Technological University, 50 Nanyang Ave, Singapore 639798, Singapore; ngvphobk08@gmail.com (V.P.N.); dhyan.bohra@gmail.com (S.B.D.)
[2] Schaeffler Hub for Advanced Research at NTU, Nanyang Technological University, 50 Nanyang Ave, Singapore 639798, Singapore
* Correspondence: wtchow@ntu.edu.sg

Abstract: Cable-driven mechanisms are increasingly popular in applications requiring low-inertia operation. However, issues like cable loosening, which leads to reduced durability and stability with long-term use, have not been fully addressed in previous studies. This paper presents a novel design for a decoupling mechanism based on the geometrical-balance principle. The mechanism incorporates three pulleys—main, minor, and guiding—mounted on a parallelogram structure. The cable passes over these pulleys and an elbow pulley with constant tension, maintained through a balance between the pulleys' radii and the cable's thickness and radius. A theoretical model was developed to estimate deviations in the cable tension within this design, considering general geometric parameters and friction coefficients. In the experimental setup, the main pulley had a radius of 15 mm, while the minor, guiding, and elbow pulleys had radii of 7 mm, and a 1 mm radius Dyneema cable was used. The results demonstrated that the decoupling mechanism maintained a consistent cable length and tension with minimal deviation as the two links rotated from small to large angles. Furthermore, a strong correlation between the theoretical estimates and experimental validation confirmed that the cable tension remained stable at both ends when the decoupling mechanism was integrated into the original system. This research improves the stability and durability of cable-driven mechanisms while offering a compact, accurate solution adaptable to a wide range of applications, including robotics, machinery, and other devices.

Keywords: decoupling mechanism; cable-driven mechanism; balance cable length; maintain cable tension; decoupling device; cable-driven robot arm; cable-driven robot hand; rope-driven mechanism

Citation: Nguyen, V.P.; Dhyan, S.B.; Chow, W.T. A Decoupling Module Based on a Geometrical-Balance Mechanism for Mitigating Cable Length Variation in Cable-Driven Applications. *Machines* **2024**, *12*, 755. https://doi.org/10.3390/machines12110755

Academic Editor: Dan Zhang

Received: 3 September 2024
Revised: 6 October 2024
Accepted: 14 October 2024
Published: 25 October 2024

1. Introduction

Cable-driven mechanisms have been widely utilized across numerous applications. In terms of manipulation, the authors of [1–5] demonstrated the advantages of rigid or hybrid gripper designs actuated by tendons/cables, particularly when compared to soft grippers made from flexible materials or mechanisms [6–9], which rely on cable tension to achieve stable grasping. Elastic cables or cords have also been employed in gripping interfaces, offering flexible tension to handle complex objects [10] or multi-object groups [11]. Cable-driven mechanisms have also been applied to reduce the operating inertia of robots such as cable-suspended robots [12], therapy platforms [13,14], parallel cable-driven robots [15], continuum robot arms [16,17], cable-driven arms [18–20], snake robots [21], human skeletons [22,23], and wearable devices [24]. In these applications, a single cable can drive the motion of one or multiple joints or links, with the magnitude and trajectory of motion dependent on variations in the cable tension. Typically, cable-driven mechanisms feature a common structure, as described in [25,26], where two cable branches rotate a link around a hinge joint.

1.1. Coupling Problem in Cables

In this paper, the cable-driven mechanism in [25,26] was simplified, as shown in Figure 1, with two links (termed link 1 and link 2) that can rotate concurrently around the center M of a hinge joint due to the tension generated by the cables. Since the two cable branches are symmetrical, we focus on the analysis model for one cable branch. Additionally, an elbow pulley with a radius r_e is mounted on the joint to guide a cable, represented by the red solid line. This cable has two endpoints, A and Z, and traverses the elbow pulley along a contact curve BC with a central angle α. In this scenario, let us assume the following: link 1 and link 2 are rigid, d_1, d_2 are constant and link 1 rotates while link 2 is stationary. When link 1 rotates around M with an angle $-\mathrm{d}\beta$, the points A and B move to new positions, i.e., $\{A^-, B^-\}$. In this scenario, α becomes $\alpha + d\beta$ and the cable is longer than its original length in the setting-up state. Also, if link 1 rotates clockwise around M with an angle of $+\mathrm{d}\beta$, points A and B move to $\{A^+, B^+\}$. Concurrently, α reduces to an amount of $\mathrm{d}\beta$ and the length of the cable reduces. Such variations in the cable length significantly change the cable tension, which causes loosening at point A and B or at the contact location: curve BC. Additionally, it becomes difficult to reach a high accuracy in controlling angle β. Thus, it is practically necessary to propose a decoupling mechanism to address these issues and enhance the performance of the cable-driven system.

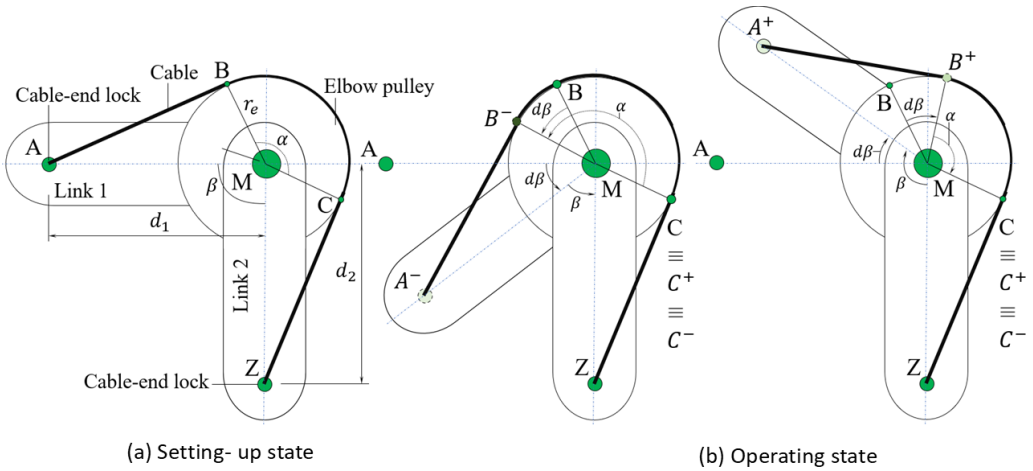

Figure 1. Schematic principle of a simple cable-driven mechanism for actuating the rotational motion of link 1 around a hinge joint M. (**a**,**b**) The illustrations of the mechanism at the setting-up (initial) and operating states, respectively. In (**a**), B and C are the starting-contact points between the cable and the pulley, and α, β are the angles BMC and AMZ. In (**b**), $\{A^+, B^+, C^+\}$ and $\{A^-, B^-, C^-\}$ are, respectively, the positions of the points A, B, C when β increases or decreases an amount of $\mathrm{d}\beta$.

1.2. Related Works on Decoupling Mechanism

Previous works have introduced various designs of decoupling mechanisms. One common approach involves inserting a spring between the cable end and the cable-end lock to automatically compensate for variations in the cable length [27–29]. Additionally, Liu [30] presented a parallelogram-decoupling mechanism that uses a cylindrical-compliant guide as a spring element to manage changes in the cable length through the spring's displacement. While this mechanism straightforwardly maintains the cable length, it suffers from lower operational accuracy due to the axial vibrations induced by the spring. Moreover, selecting an appropriate spring with the correct stiffness becomes a challenge, especially in applications with large deviations in the payload. More recently, decoupling mechanisms using a cable-wound base have gained attention. For example, the authors in [31] theoretically proposed a decoupling mechanism for driving a jaw gripper, which uses planetary gear transmissions and pulley systems as the core structure. Similarly, Surong [26] introduced a novel decoupling mechanism based on a cable-wound system. However, significant variations in the cable tension were still observed when changing

angle α, and friction forces between the two cable ends had a considerable impact on the tension.

Our study presents a novel design for a decoupling mechanism that effectively maintains both the length and tension of the cable by leveraging a balanced geometrical configuration. The mechanism consists of three pulleys: minor, main, and guiding, all mounted on a parallelogram assembly. The cable runs through these pulleys and automatically compensates for length variations through geometrical adjustments. A theoretical model was developed to analyze the effects of geometrical parameters and friction on deviations in the cable length and tension between the two cable ends. Based on this model, the decoupling mechanism was designed, and experiments were conducted to validate the theoretical findings. The contributions of this paper include the following: (1) proposing a novel decoupling mechanism design that minimizes cable length variation during rotation, addressing the issues identified in [26,31]; (2) reducing axial vibrations along the cable, overcoming the challenges outlined in [27–30]; (3) minimizing tension deviations between the two cable ends caused by friction; and (4) enabling the mechanism to accommodate multiple cables without creating a bulky structure.

2. Design of Decoupling Mechanism

2.1. Principle Design

In Figure 1, in the initial state, the length of the cable l_c is the sum of the line/curve: AB (l_{AB}), BC (l_{BC}), and CZ (l_{CZ}). Hence, the change in l_c is an entity depending on β, in other words, we have

$$\Delta l_c = r_e d\beta. \tag{1}$$

To eliminate the variation in $r_e d\beta$ in Equation (1), a novel principle for the decoupling mechanism is designed, as illustrated in Figure 2. In this scenario, the decoupling configuration includes three pulleys: main, minor, and guiding, with their center shafts located at N and J, respectively. The center N is located between the line MZ and far from M at a distance of d_4 ($d_4 < d_2$). Further, L, and K, are the centers of the hinge joints at their locations, positioned at a distance of d_3 with $d_3 < d_1$ from line MZ. Link JKN (termed the driving link) is used to drive a parallelogram mechanism, KLMN ([32,33]), via a connecting link, KL. To ensure the decoupling works normally, $d_5 + r_g$ is smaller than $d_2 - d_4$. After mounting the decoupling mechanism, from C, the cable travels to the main pulley, guiding pulley, and minor pulley before ending at Z in a trajectory $D \to E \to F \to G \to G \to H \to I \to Z$. In this situation, the cable length additionally appends other lines such as $l_{CD}, l_{DE}, l_{EF}, l_{FG}, l_{GH}, l_{HI}, l_{IZ}$, determined as follows:

$$\begin{bmatrix} l_{CD} \\ l_{DE} \\ l_{EF} \\ l_{FG} \\ l_{GH} \\ l_{HI} \\ l_{IZ} \end{bmatrix} = \begin{bmatrix} 0 & 0 & 0 & 0 & 0 & 1 \\ \theta & 0 & 0 & 0 & 0 & 0 \\ 0 & 0 & \sin\psi_3 & 0 & 0 & 0 \\ 0 & 0 & 0 & \vartheta & 0 & 0 \\ 0 & 0 & \sin\psi_4 & 0 & 0 & 0 \\ 0 & 0 & 0 & 0 & \gamma & 0 \\ 0 & 0 & 0 & 0 & 0 & \sin\psi_5 \end{bmatrix} \begin{bmatrix} d_4 \\ r_b \\ d_5 \\ r_g \\ r_m \\ d_6 \end{bmatrix}. \tag{2}$$

In Equation (2), the entities ψ_3, ψ_4, and ψ_5 are, respectively, calculated at $\arccos[(r_b - r_g)/d_5]$, $\arccos(r_m/d_5)$, and $\arccos(r_m - r_g)/d_5$, which are the constant values. Hence, when the driving link rotates around N, there is no variation in the angles and edge lengths of the polygon GHNEFJ. In other words, the angle ϑ is always a constant and the elements in the left-hand side of Equation (2) depend on the angles θ and γ. According to the explanation in the model of Figure 1, when A travels to position A^+, we have the lengths l_{BC} and l_{HI}, respectively, reducing an amount of $r_e d\beta$ and $r_m d\beta$, whereas l_{DE} increases an amount of $r_b d\beta$. By combining Equations (1) and (2) Δl_c with the inclusion of the decoupling mechanism, this can be deduced as follows:

$$\Delta l_c = d\beta(r_e - r_b + r_m). \tag{3}$$

In Equation (3), the value of Δl_c has the signs "+" or "−" with respect to the motion of A to A^+ or A^-, respectively. Also, Δl_c varies with the radius of the pulleys and is completely independent of distance parameters such as d_1, d_2, d_4, d_5, d_6. To eliminate the deviation of the cable length, the value of Δl_c in Equation (3) has to become zero. Therefore, Equation (3) is transformed into Equation (4):

$$r_b = r_m + r_e. \tag{4}$$

Equation (4) enables the design of the pulley system dimensions before its installation on the mechanism shown in Figure 1 under the assumption that only the geometry is considered, and the thickness of the cable t_c is ignored. In real conditions, each nominal dimension r_e, r_m, r_b is always accompanied by a corresponding dimension tolerance of D_e, D_m, D_b and a shape tolerance of S_e, S_m, S_b after machining. Assuming that S_r, S_m, S_b can be ignored, the nominal dimensions r_e, r_m, r_b are replaced by the actual dimensions R_e, R_m, R_b, which are calculated at $r_e + D_e, r_m + D_m, r_b + D_b$. In other words, the relation in Equation (4) can be presented by R_e, R_m, R_b, and t_c in Equation (5):

$$R_b = R_m + R_e + t_c. \tag{5}$$

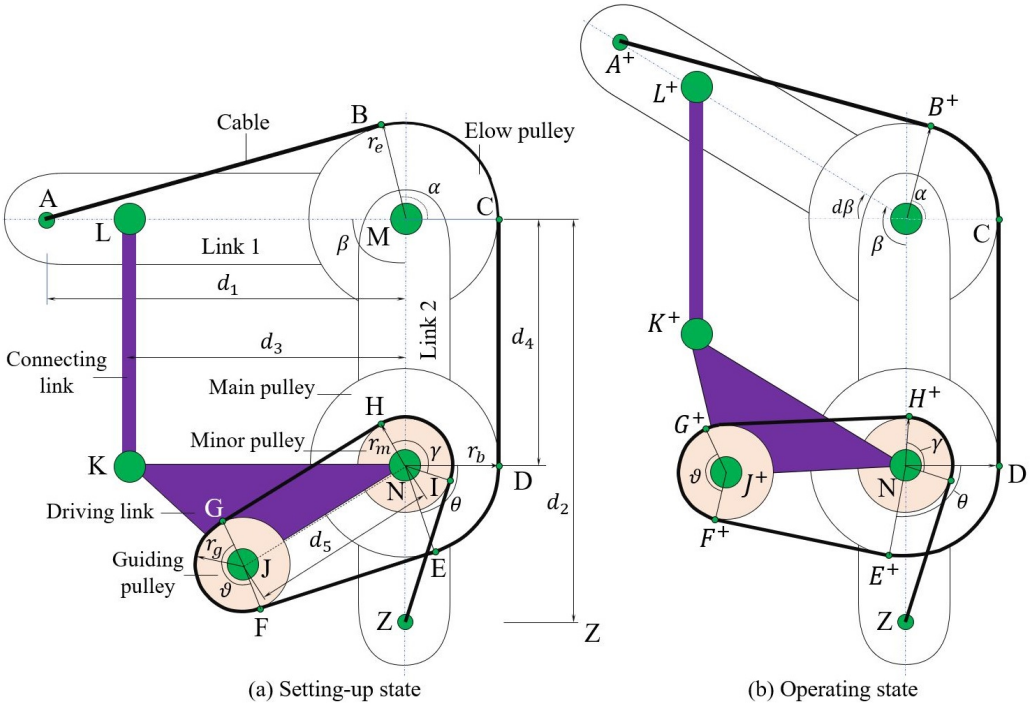

Figure 2. Schematic illustration of decoupling mechanism with the pulley-based system in setting-up state (**a**) and operating state (**b**). In this figure, r_e, r_b, r_m, r_g are the radii of the elbow, main, minor, and guiding pulleys, respectively. B, C, D, E, F, G, H, and I are the points where the cable makes contact with the pulleys. Also, γ, θ, and ϑ are the central angles on the minor, main, and guiding pulleys, respectively. I, J, and K are on the same link (termed the driving link).

2.2. Influence of Decoupling Mechanism to Structure Kinematic

Attaching the decoupling mechanism to the rotational mechanism in Figure 1 can maintain the cable length during operation. However, the cable in this scenario has to traverse through a system comprising multiple pulleys. This may cause a reduction in the cable tension at A and Z. In the setting-up state in Figure 3a, the cable tension at two neighbour points, outside the contact areas with the pulley, have the same magnitudes, for instance, $T_A = T_B$, $T_C = T_D$, $T_E = T_F$, $T_G = T_H$, and $T_I = T_Z$. At the contact locations with the pulleys, due to the influence of friction, the tensions between two neighbour points are different by an amount of $e^{\mu\phi}$, according to the Capstan equation [34,35]. Additionally, if

the pulleys rotate around the hinge joints, the deviation entity $e^{\mu\phi}$ reduces by the rolling coefficient η. Hence, the difference in the cable tension at the pulley-contact areas can be calculated using Equation (6):

$$\begin{Bmatrix} |\Delta T_{BC}| = |T_B - T_C| \\ |\Delta T_{DE}| = |T_D - T_E| \\ |\Delta T_{FG}| = |T_F - T_G| \\ |\Delta T_{HI}| = |T_H - T_I| \end{Bmatrix} = \begin{bmatrix} \eta_\alpha \\ \eta_\theta \\ \eta_\varphi \\ \eta_\gamma \end{bmatrix} \begin{bmatrix} e^{\mu_\alpha \alpha} - 1 \\ e^{\mu_\theta \theta} - 1 \\ e^{\mu_\vartheta \vartheta} - 1 \\ e^{\mu_\gamma \gamma} - 1 \end{bmatrix} \begin{Bmatrix} T_B \parallel T_C \\ 3T_D \parallel T_E \\ T_F \parallel T_G \\ T_H \parallel T_I \end{Bmatrix}. \quad (6)$$

In Equation (6), the variations in the cable tensions depend on the friction coefficients, (i.e., μ) and the sweep angle ϕ, whereas other parameters relating to the pulley size do not affect this. The sign of such variations is with respect to the correlative motion between the cable and the pulley. Let us transform Equation (6) into $\Delta T = \Psi T$, where T is the matrix comprising the smaller elements in each row. The function Ψ is directly proportional to the μ group: μ_α, μ_θ, μ_φ, μ_γ; the η group: η_α, η_θ, η_φ, η_γ; and the angles: α, θ, φ, γ (see Figure 4). When there is no rolling motion between the pulley and the hinge shaft, (i.e., $\eta = 1$), Ψ reaches a maximum value of 15.3 at $\mu = 0.9$ and $\alpha = \pi$. This value drops to 1.53 and 0.153, corresponding with $\eta = 0.1$, and 0.01, respectively. The influence of Ψ in Equation (6) can be eliminated as η and μ approach close to zero or α becomes infinitesimal. At the operating state (see Figure 3b), as point A moves to A^+ position, the cable shifts from C to D, and from G to F. In this scenario, applying Equation (6) to each contact location, we can obtain $T_C = T_B[\eta_\alpha(e^{\mu_\alpha \alpha} - 1) + 1]$, $T_E = T_D[\eta_\theta(e^{\mu_\theta \theta} - 1) + 1]$, $T_F = T_E[\eta_\vartheta(e^{\mu_\vartheta \vartheta} - 1) + 1]$, and $T_H = T_I[\eta_\gamma(e^{\mu_\gamma \gamma} - 1) + 1]$. Hence, the relation between the cable tension between points A^+ and Z can be shown as follows:

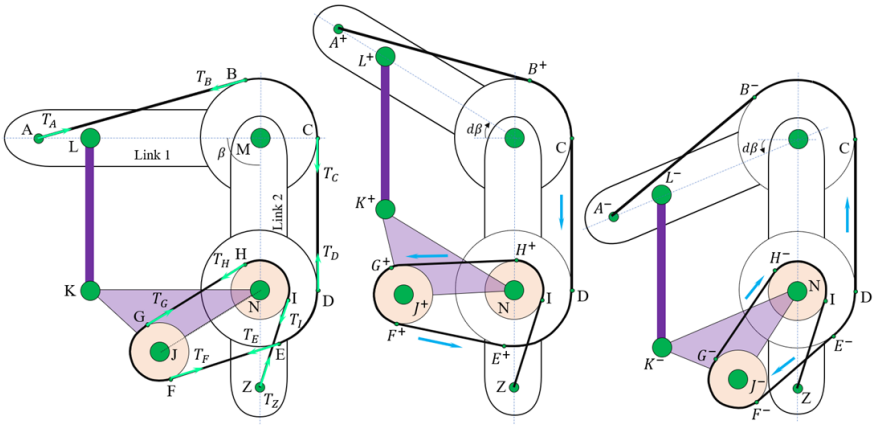

Figure 3. Kinetics analysis of the cable tension in setting-up (**a**) and operating (**b**) states. T_A, T_B, T_C, T_D, T_E, T_F, T_G, T_H, T_I, and T_Z are, respectively, the cable tension at each starting-contact point. The blue arrows indicate the local motions of the cable at each line according to the rotating direction of link 1.

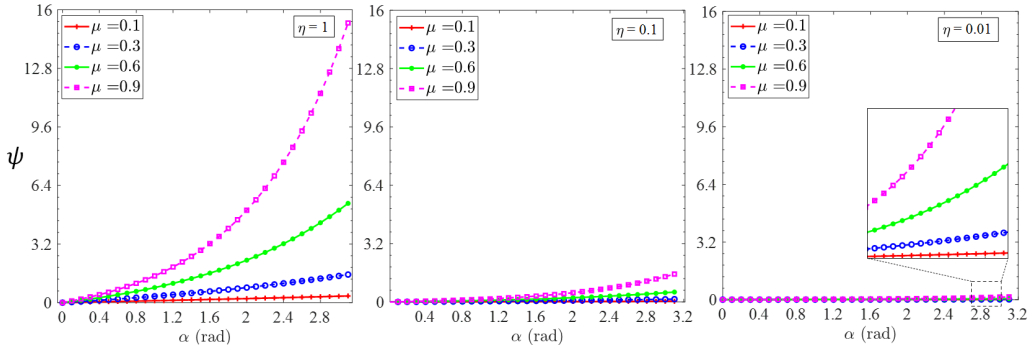

Figure 4. Estimation of ψ by the variation in μ, and α according to three levels of η = 1, 0.1, and 0.01. In this scenario, we can replace α with other angles such as θ, ϑ, and γ to calculate ϕ in such cases. See Table 1 for the numerical value of ψ in the cases of $\eta = 0.1$ and 0.01.

Table 1. ψ value of $\eta = 0.1$ and 0.01 at $\alpha = 3.1$.

η	μ = 0.1	μ = 0.3	μ = 0.6	μ = 0.9
0.1	1.53	0.54	0.15	0.04
0.01	0.15	0.05	0.02	0.004

$$\frac{T_{A^+}}{T_Z} = \frac{[\eta_\gamma(e^{\mu_\gamma(\gamma - d\beta)} - 1) + 1][\eta_\vartheta(e^{\mu_\vartheta \vartheta} - 1) + 1]}{[\eta_\theta(e^{\mu_\theta(\theta + d\beta)} - 1) + 1][\eta_\alpha(e^{\mu_\alpha(\alpha - d\beta)} - 1) + 1]}. \quad (7)$$

Concurrently, when A moves to A^-, the relation in Equation (7) becomes

$$\frac{T_{A^-}}{T_Z} = \frac{[\eta_\alpha(e^{\mu_\alpha(\alpha + d\beta)} - 1) + 1][\eta_\theta(e^{\mu_\theta(\theta - d\beta)} - 1) + 1]}{[\eta_\gamma(e^{\mu_\gamma(\gamma + d\beta)} - 1) + 1][\eta_\vartheta(e^{\mu_\vartheta \vartheta} - 1) + 1]}. \quad (8)$$

Equations (7) and (8) prove that the ratio between T_A and T_Z varies according to the change in angle dβ and the moving direction of point A. Additionally, this ratio depends on the frictional coefficients from the μ and η groups.

2.3. Three-Dimensional Model of the Decoupling

The decoupling mechanism described in Figure 3 was designed for carrying out experiments. To drive link 1, one motor was mounted with its center shaft coinciding with N. As shown in Figure 5, link 1 was a bar with one end rotated around shaft 2 having its center line coincident with M (in front view). This shaft was also the joint between link 1 and panels 1 and 2. The remaining end of this link was connected with connecting link LK via shaft 1. The driving link JKN comprised two symmetrical plates (plate 1 and plate 2) with N and J being the centers of shaft 3 and shaft 5. One end of this link was connected with the connecting link via shaft 4, whereas the remaining end had different connections, i.e., plate 1 rotating around shaft 3 and plate 2 fixing a motor shaft. The pulley group included four pulleys: the elbow pulley on shaft 2, the minor and main pulleys on shaft 3, and the guiding pulley on shaft 4. The cable was locked at A and traversed through the pulley system before being terminated at Z at the bottom. The mounting trajectory of the cable was similar to that shown in the illustration in Figure 2. The decoupling mechanism was attached to a standing structure through shaft 3 and the motor. This structure included link 2, which was mounted on a jig. Link 2 consisted of two panels, panel 1 and panel 2, which supported the parallelogram mechanism integral to the decoupling system. As the motor rotated, it activated the driving link JKN, which in turn drove the motion of both the connecting link KL and link 1. Throughout this process, the cable length was automatically maintained by the decoupling mechanism.

From the design in Figure 5, we have the value of the angles at $\beta = 56.5°$ as follows: $\alpha = 122.7°$, $\theta = 65°$, $\vartheta = 176.1°$, and $\gamma = 123.5°$. The variation in the cable tension between two cable locks A and Z depends on the position of link 1 with link 2. Hence, the range of dβ = [0,1.4] (rad), which means β = [0.99,2.39] (rad), is the main parameter for investigating

the kinematics model of the decoupling mechanism. Let us estimate the tension ratio T_A/T_Z in the case of link 1 rotating in the clockwise direction corresponding with Equation (7) and the friction coefficients being the same for each group, i.e., μ and η for the μ and η groups, respectively. Figure 6 shows the relation of T_A and T_Z after applying parameters from the design into Equation (7). In this scenario, the ratio is a positive covariance with μ and rapidly increases when $\mu \rightarrow 0.9$, whereas it displays inverse covariance with dβ. The maximum and minimum values of T_A/T_Z are, respectively, at $\{d\beta, \mu\} = \{0, 0.9\}$, and $\{d\beta, \mu\} = \{1.4, 0.1\}$ in each inset graph. Additionally, T_A/T_Z becomes closer to 1 when η reduces to zero. In other words, the tension loss in the cable is insignificant if the pulleys rotate or the contact interfaces between the cable and the pulleys are smooth. By applying the estimation of Equation (7) with the same input parameters into Equation (8) with link 1 reversing its moving direction, we can achieve a similar theoretical conclusion.

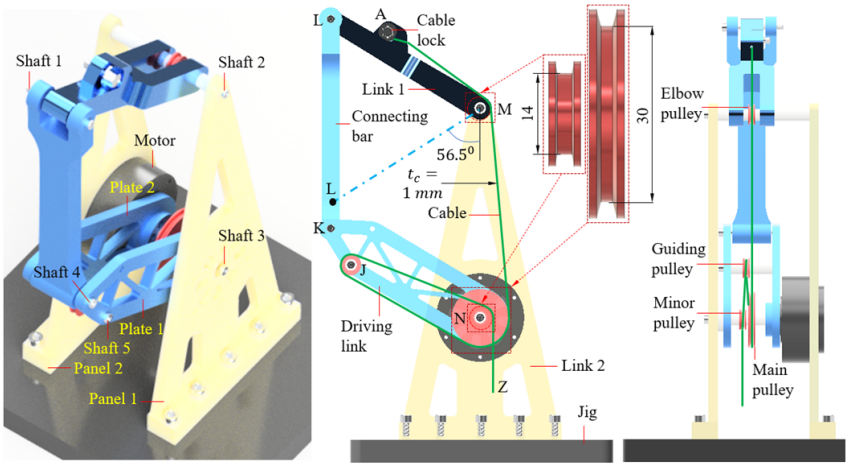

Figure 5. Three-dimensional design of the decoupling mechanism mounted on a stand system in (**a**) isometric view, (**b**) front view, and (**c**) side view. The blue dash-dotted line indicates the lowest position of link 1 corresponding with an angle of 56.5° from the horizontal line. In this design, we ignored $r_m = r_e = 7$ mm, and concurrently, $r_b = 15$ mm, and $t_c = 1$ mm.

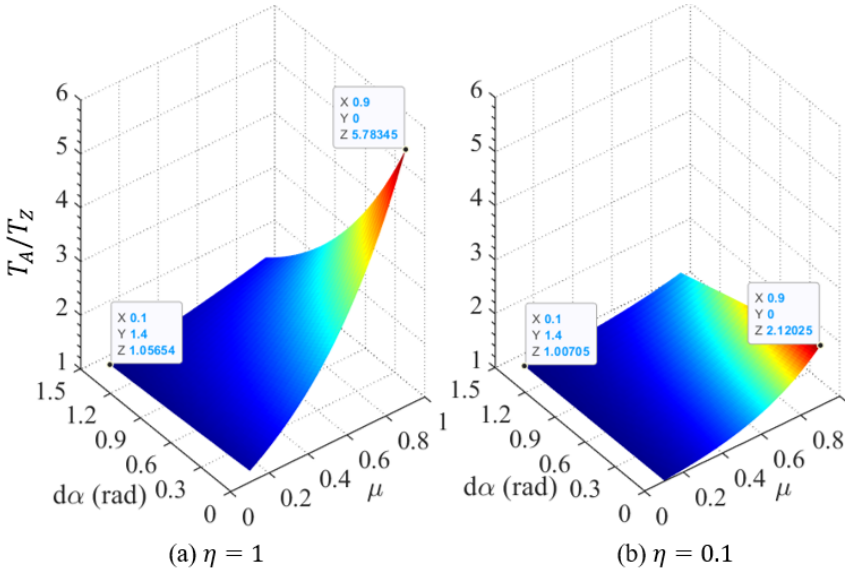

Figure 6. *Cont.*

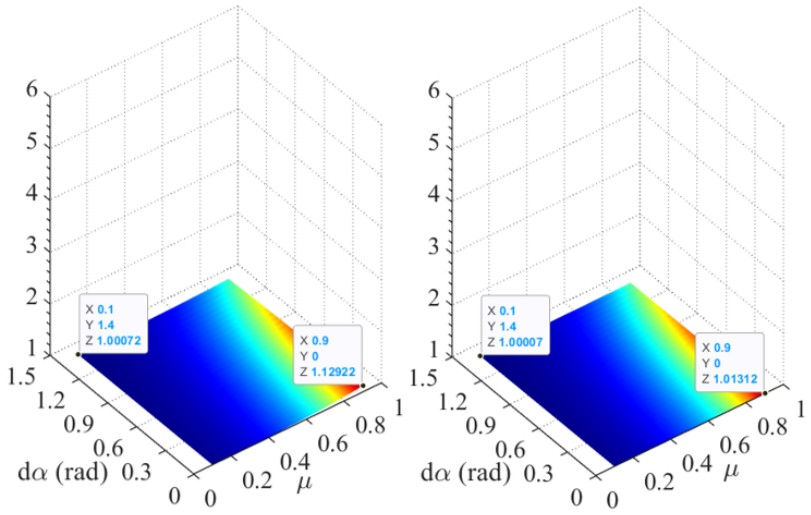

(c) $\eta = 0.01$ (d) $\eta = 0.001$

Figure 6. Influence of the parameters $d\beta, \mu$ on the tension ratio T_A / T_Z at four levels of η (**a**) 1, (**b**) 0.1, (**c**) 0.01, and (**d**) 0.001. These graphs were obtained from Equation (7) with the angle parameters originating from Figure 5.

3. Results

3.1. Experimental Setup

As shown in Figure 7, the panels are made from PLA plastic and printed using the in-house Anycubic Kobra Max 3D printer. The experimental setup utilizes a set of four 3D-printed pulleys: the elbow pulley, minor pulley, main pulley, and guiding pulley. Shaft 3 is connected to an RMD-X6 motor, which powers the entire decoupling mechanism. The motor shaft is linked to the two panels of link 2, which are, in turn, connected to the driving link. Additionally, the driving link is attached to a connecting link bar, rotating in sync with the motor shaft's movement. The entire mechanism uses a Dyneema fiber cable of 2 mm radius ($t_c = 1$ mm) routed through the pulleys. One end of the cable is fixed to link 1, while the other end is attached to a hook at the end of a digital force gauge. The force gauge used has a range of 50 N to measure the tension force on the cable.

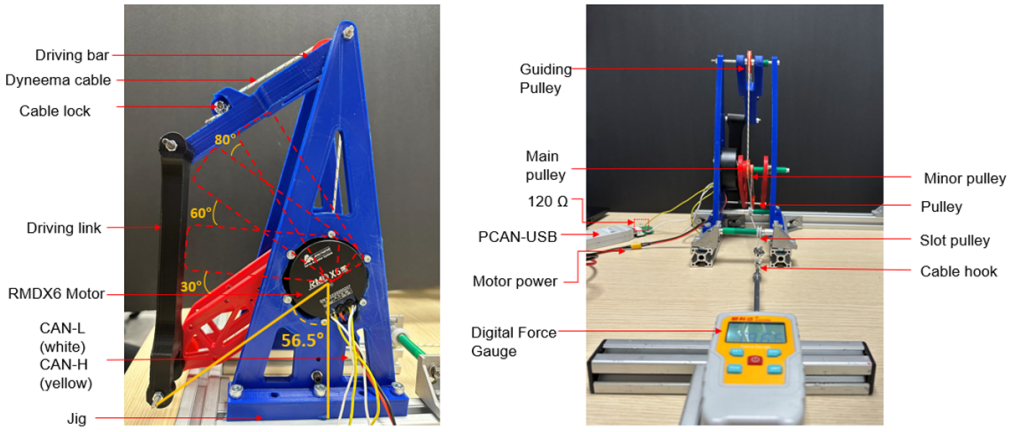

(a) Front view (b) Side view

Figure 7. Experimental setup for the novel decoupling mechanism with a digital force gauge sensor shown in (**a**) front view and (**b**) side view. The dashed line in (**a**) the front view represents the position of the plates attached to the motor when the shaft rotates through angles of 30°, 60°, and 80°.

3.2. Electrical Design and Control

The decoupling mechanism is actuated using the RMD-X6 high-precision, lightweight, and compact servo motor. The motor has a reducer ratio of 6:1 and operates at an input

voltage of 24–48 V to perform functions based on the load on the motor. In our experiments, we use a nominal voltage of 48 V to power the motor. The motor uses a robust standard protocol of communication, i.e., CAN (Controller Area Network) bus protocol, to receive commands from the host computer and perform the desired action. This communication is carried out using the PCAN-USB adapter developed by PEAK-System, which enables high-speed CAN communication up to bit rates of 1 Mbit/s. A bus termination of 120 Ω is soldered between the CAN High and CAN Low terminals on the PCAN. The CAN monitor PCAN-View 5 software on Windows is used for transmitting and viewing the CAN messages. The design of the communication and control is as illustrated in Figure 8.

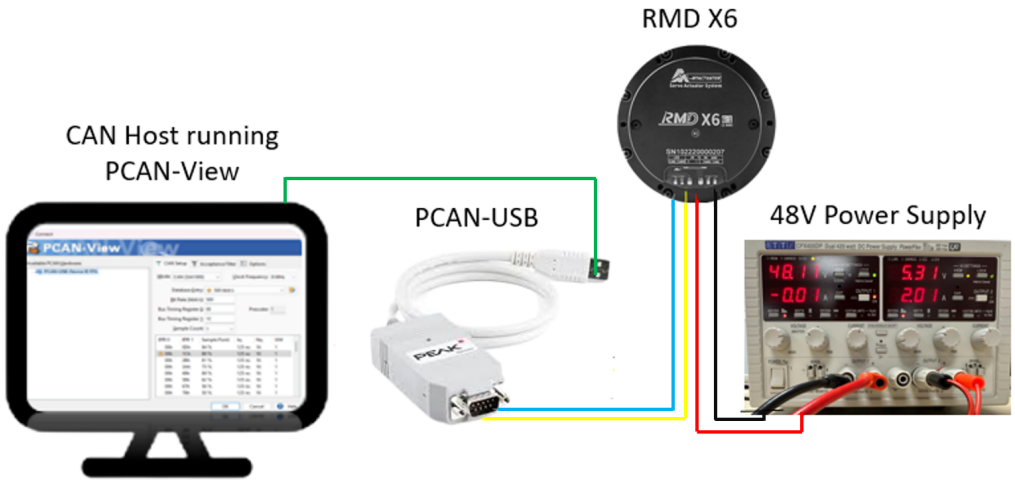

Figure 8. Schematic illustration of electrical design and control for a novel decoupling mechanism.

3.3. Decoupling Mechanism Force Test

Experiments were conducted to analyze the tension on the Dyneema cable in the decoupling mechanism (see Figure 7). The set of pulleys used for the experiments have radii of 15 mm for the main pulley and 7 mm for the minor/elbow/guiding pulley. The cable has one end locked at the cable lock on the driving bar, whereas the other end is hooked at the digital force gauge, which documents the tension value of the cable in real time. Before running the motor shaft, the decoupling mechanism setup is pre-tensioned to three sets of forces of 5 N, 20 N, and 30 N as measured using the digital force gauge. Starting from the initial position of the driving link at 56.5° from the vertical line, the motor shaft makes the mechanism rotate with dβ of 0°, 30°, 60° and 80°, as shown in Figure 7. Furthermore, experiments were conducted with four sets of motor speeds of 15 dps, 30 dps, 60 dps and 120 dps.

Figure 9 shows line plots of the forces measured on the Dyneema cable at angle dβ, where the decoupling mechanism is under tensions of 5 N, 20 N, and 30 N. Each line further represents the results at four sets of motor speeds at which the forces are measured when the mechanism moves through the angles. As seen from the graph for the mechanism under a tension of 5 N, the maximum force measured is 5.5 N at 80° and the minimum force measured is 4.4 N at 30°, which is a deviation of +10% and −12%. For the mechanism under a tension of 20 N, the maximum force measured is 20 N at the initial position of 0°, and the minimum force measured is 15.5 N at 30°, which is a deviation of −22.5%. Lastly, at a tension of 30 N, the maximum force is 30 N measured at 0°, whereas the minimum force measured is 24.6 N at 30°, which is a deviation of 18%. It can be inferred from the three plots that the minimum force measured across all the experiments is that when the decoupling mechanism is at 30°. This can be explained by the fact that, at 30°, as shown in Figure 7, the mechanism is horizontally aligned and nearly parallel to the surface. This generates the maximum axial compression on the driving links and the maximum shear force on shaft 5. Such forces pull J nearer to N by reducing the tolerance gap between the assembly parts. Based on Equation (2), decreasing d_5 led to shortening l_{DE}, l_{EF}, l_{FG}, and

l_{GH}. Since the total length of the cable is unchanged, the cable is slightly more loosened at this angle than at other angles, resulting in the minimum force measured.

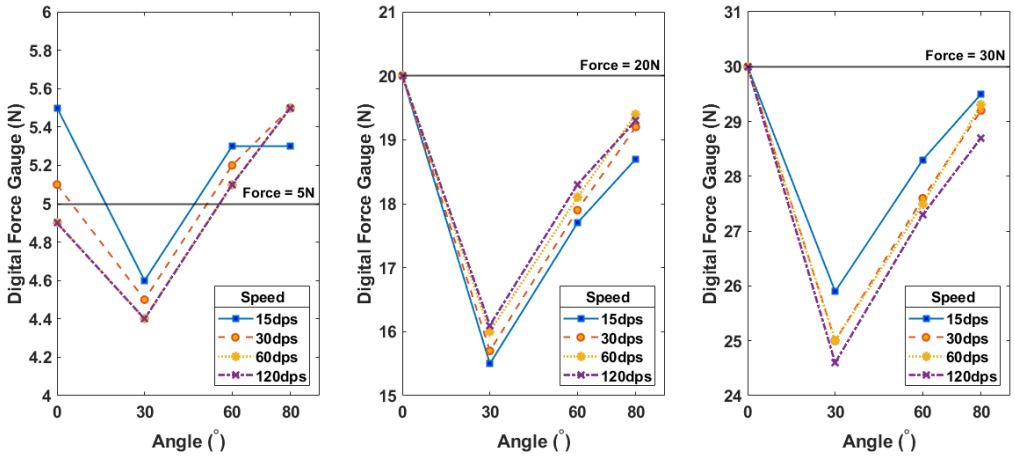

Figure 9. Graphical representation of forces measured on the Dyneema cable at the angle d$\beta = 0°$, 30°, 60° and 80°. The forces are measured when the system is under the cable tension of 5 N, 20 N and 30 N.

In Figure 10 under a tension of 5 N, it can be seen that the forces measured at 80° at different speeds are the highest, while at 30° they are the least. When the decoupling mechanism is under a tension of 20 N, at the initial stage of 0°, the forces are highest, whereas at 30°, for all the speeds, they are the least. The general trend is for the force on the cable to be lower for lower speeds of 15 dps and 30 dps. Lastly, under a tension of 30 N the forces measured at 30° are lowest for all the speeds of the motor. The general trend observed is for a particular angle. The force measured at a speed of 15 dps is the highest, and on the other hand, for 120 dps, it is the lowest.

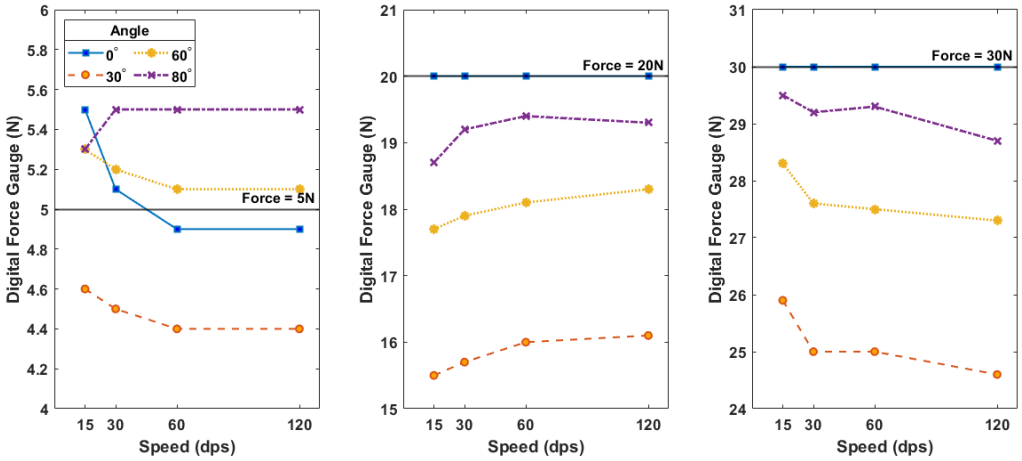

Figure 10. Graphical representation of forces measured on the Dyneema cable at 15 dps, 30 dps, 60 dps, and 120 dps. The forces are measured when the system is under the tensions of 5 N, 20 N, and 30 N.

In Figure 11, the value of each bar is the mean force value calculated when the mechanism is traveling at different speeds of the motor. The error bars represent the standard deviation of the set of forces measured for different speeds of the motor, for a particular angle. For the decoupling mechanism at a position of 30°, the maximum error of ∓ 0.55 N, is for the system under 30 N. Similarly, for the angles of 60° and 80°, the maximum error of ∓ 0.434 N and ∓ 0.34 N, respectively, is when the system is under a tension of 30 N. Across different angles, as explained earlier and as can be seen from the chart, the maximum error is for 30°. From Figure 11, we can also infer that at 80°, the system behaves most similarly to the true force values with the least errors.

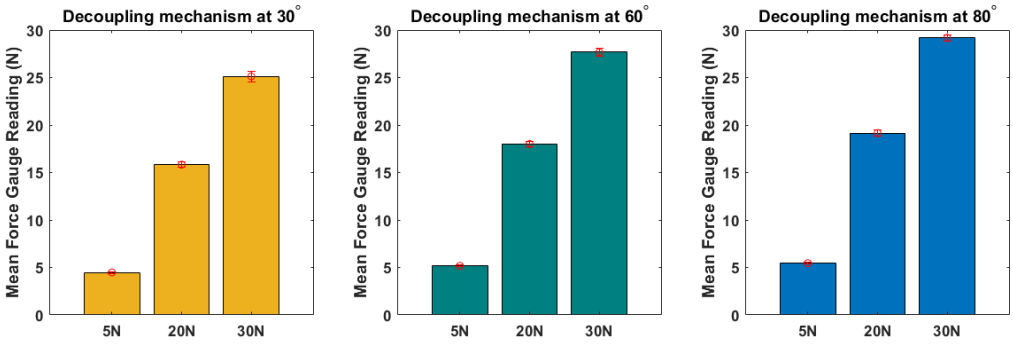

Figure 11. Mean force gauge reading and standard deviation of forces measured for the system at angles of 30°, 60°, and 80°.

In Figure 12, the error bars represent the standard deviation of the set of forces measured for different angles of the mechanism at a particular speed. At a speed of 15 dps, the least error is ∓0.394 N when the system is under 5 N of force and the highest error is ∓1.899 N when the system is under 20 N of force. At a speed of 30 dps, the least error is ∓0.419 N when the system is under 5 N of force and the highest error is ∓2.2053 N when the system is under 30 N of force. A similar trend follows suit for the decoupling mechanism at 60 dps and 120 dps, where the minimum error is for the forces measured at 5 N and the maximum error is for the forces measured at 30 N. From the plot, it can also be inferred that the mean force gauge reading measured at 5 N is the closest to the true value for all the speeds of the decoupling mechanism. The deviation tension T_Z was slightly different at $d\beta_{min} = 0$ and $d\beta_{max} = 1.4$. Concurrently, the variation in the motor speed generated was slightly different on T_Z. Thus, our decoupling mechanism did not generate any significant change in the cable tension at A and Z under diverse conditions of load and velocity.

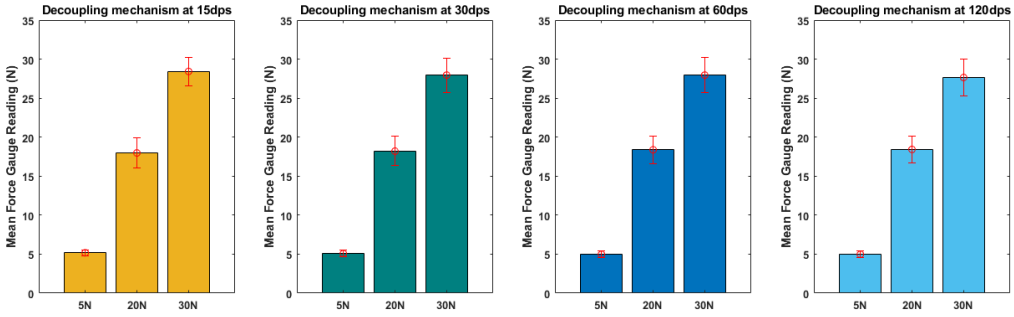

Figure 12. Mean force gauge reading and standard deviation of forces measured for the system at speeds of 15 dps, 30 dps, 60 dps, and 120 dps.

3.4. Non-Decoupling Mechanism Force Test

In Figure 13, we can see three perspectives of the experimental setup for a non-decoupling mechanism. For this mechanism, there is only one main pulley used in addition to the guiding pulleys. The main shaft is connected to an RMD-X6 motor, which drives the entire decoupling mechanism. The entire mechanism uses a cable of Dyneema fiber of 2 mm thickness routed through the main pulley and guiding pulleys. One end of the cable is fixed to the driving link, while the other end is attached to a hook at the end of a digital force gauge. The force gauge used has a range of 500 N to measure the tension force on the cable.

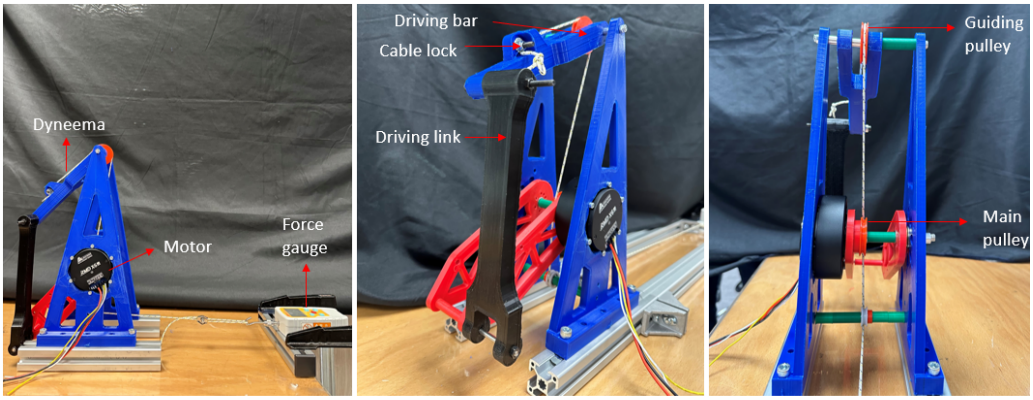

(a) Front view (b) Isometric view (c) Side view

Figure 13. Experimental setup for a non-decoupling mechanism with a digital force gauge sensor shown in (**a**) front view, (**b**) isometric view, and (**c**) side view.

The results obtained from the experiments are shown in Table 2 below. Similar to the decoupling mechanism force tests, the system was subjected to three sets of forces: 5 N, 20 N, and 30 N. In addition, the mechanism was also made to move through 0°, 30°, 60°, and 80°. At the highest angle, that is, 80°, the Dyneema cable measures the forces of 4.5 N, 21 N, and 32 N, which are approximate to the initial system load. As the mechanism is made to move downwards to 60°, 30°, and 0°, the digital force gauge readings increase. At 0°, the forces are at a maximum of 210 N, 270 N, and 370 N for the three sets of system loads of 5 N, 20 N, and 30 N, respectively. Naturally, when the system is under a load of 30 N, the forces measured at the same angles, in comparison, are relatively higher than those for 5 N and 20 N.

Table 2. Force readings between non-decoupling mechanism vs. decoupling mechanism.

Angle	Force = 5	Force = 20	Force = 30
0°	210 | 5.5	270 | 20	370 | 30
30°	136 | 4.6	153 | 15.5	300 | 25.9
60°	27 | 5.3	63 | 17.7	150 | 28.3
80°	4.5 | 5.3	21 | 18.7	32 | 29.5

Table 3 below shows the % breaking strain force on the Dyneema cable when the system is subjected to loads of 5 N, 20 N, and 30 N. The Dyneema cable used for the experiments has a peak load of 200 kg (or 1961.33 N). When the driving link is at 80°, the % strain on the Dyneema cable is under 2%. As the system is subjected to higher loads, the cable is consequently subjected to larger strains. The strain on the Dyneema cable is at its highest of about 18.9% when the mechanism is at 0° and the initial system tension is 30 N.

Table 3. % breaking strain on the Dyneema cable for non-decoupling mechanism vs. decoupling mechanism.

Angle	Force = 5 N	Force = 20 N	Force = 30 N
0°	10.7% | 0.3%	13.8% | 1%	18.9% | 1.5%
30°	6.9% | 0.2%	7.8% | 0.8%	15.3% | 1.3%
60°	1.4% | 0.3%	3.2% | 0.9%	7.6% | 1.4%
80°	0.2% | 0.3%	1.1% | 1%	1.6% | 1.5%

From the comparisons in Tables 2 and 3, in the non-decoupling mechanism, both the cable tension and breaking strain are significantly higher than in the decoupling mechanism, leading to two key issues. First, if the cable is fully clamped at the locks and the system is rigid, the cable undergoes greater elongation, resulting in control inaccuracies and

reduced cable durability. Second, if the cable stiffness exceeds that of the system, the increased tension can loosen the cable locks or even damage the system. Our proposed decoupling mechanism addresses these issues, offering a solution superior to that of systems lacking any decoupling mechanisms. Compared to previous designs using spring-based decoupling mechanisms, our approach eliminates vibration along the cable by using geometrical compensation. However, one challenge is that our design requires high precision in the fabrication and assembly processes, such as in the pulley radii and the distances between the shafts. This issue will be discussed in the next subsection.

3.5. Influence of the Dimension Tolerance on the Cable Length

The accuracy of the pulley radii significantly impacts the efficiency of the decoupling mechanism. This issue was discussed in Equation (5), with the results presented in Figure 14. In this analysis, the variation in the cable length Δl_c was estimated across a range of dβ with four levels of tolerance in the pulley radii D_b: 0.01, 0.1, 0.2, and 0.3 mm. As shown in Figure 14a, when dβ increased by 1.4 rad, Δl_c grew by 0.014, 0.14, 0.28, and 0.42 mm, respectively, in direct proportion to D_b. Conversely, when the main pulley radius was smaller (D_b was negative), Δl_c decreased by the same amounts of 0.014, 0.14, 0.28, and 0.42 mm as D_b increased with an inverse relationship to dβ. The deviation in the cable length directly affects cable tension. Dyneema cable, with its high stiffness and Young's modulus of around 60 to 110 GPa, can be considered to exhibit non-elongation under tension. However, even minor deviations in Δl_c, depending on the system stiffness and tightness of the cable locks at A and Z, could result in loosening or motor overload. Therefore, in practice, achieving higher pulley precision minimizes tension variation. For cables with lower stiffness, elasticity can help compensate for geometrical inaccuracies in the mechanism, offering some flexibility.

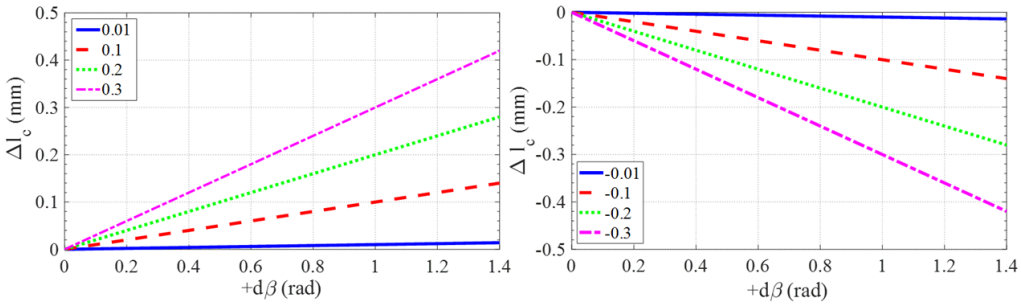

(a) Positive sign (+) of the tolerance (b) Negative sign (-) of the tolerance

Figure 14. Influence of tolerance D_b on the cable length variation Δl_c when changing angle β. In this figure, four levels of D_b are (**a**) 0.01, 0.1, 0.2, and 0.3 mm with a positive sign and (**b**) -0.01,-0.1, -0.2, and -0.3 mm with a negative sign input for the investigation. The estimated outcomes were obtained by applying the parameters from the design in Figure 5 to Equation (5).

The theoretical model in Equation (2) indicates that the dimension of the mechanism including d_1, d_2, d_3, d_4, d_5, and d_6 is independent of the variation in Δl_c. This can be applied in terms of S_r, S_m, S_b closing to zero. The shape tolerances S_r, S_m, S_b always exist, with their magnitudes depending on the fabrication methods. Thus, the influence of such dimensions needs to be considered after fabricating the pulleys. Also, the mechanism dimensions determine the value of the angles $\{\alpha, \theta, \vartheta, \gamma\}$ that affect the ratio in Equations (7) and (8).

3.6. Influence of Friction on the Cable and Controlling System

In cable-driven applications, the friction between the cable and its contact components significantly influences the durability of the cable, the operation lifetime, and the power of the actuators. For instance, the Bowden cable in [36–40] facilitates a reduction in the number of pulleys or string cords/cables, and in [41,42], it eliminates another spring element. However, the friction force between the cable and the path cover, the pulley,

and the shaft is very large, causing abrasion in the cable, especially under a heavy load and motions at high speed. Hence, after short-term usage, users have to adjust the cable tension due to the reduction in cable durability. The main challenge is to maintain the controllable accuracy of the cable-driven mechanism. Our decoupling mechanism tackles such problems with the help of the rolling pulley system that transforms sliding friction into rolling friction on the cable (see the estimation in Figure 6). In other words, the influence of friction in this mechanism may be neglected.

In summary, the decoupling mechanism proposed in this study can prevent the cable from changing its length when angle β varies with different velocities and pre-tension. By inverting the mounting direction of the cable, this model is also appropriate to the opposite cable branch in Figure 1. Thus, it is useful for a wide range of applications including cable-driven systems, as introduced in Section 1. Using a geometry-based mechanism to compensate for cable length can improve the stiffness of cable-driven systems. This is because the tension depends on the cable's stiffness, which is an advantage over spring-based decoupling mechanisms. However, our mechanism requires high precision in fabrication and assembly, along with low friction on the pulleys—such requirements that may not be as critical in spring-based mechanisms.

4. Conclusions

This paper presents a novel decoupling mechanism designed to maintain a consistent cable length across a hinge joint, based on a geometrical structure. The mechanism was analyzed theoretically and tested experimentally to evaluate the effects of friction and geometrical precision on the cable length and tension variations. The experimental findings demonstrated that the decoupling mechanism effectively preserves both the cable length and tension as the two links rotate around the hinge joint. The variations in the cable tension were minimal, showing slight changes with angle β and the rotational speed of the driving link, which closely matched the theoretical predictions. This study found that the cable tension fluctuations were mainly influenced by the accuracy of the pulley radii, while the friction losses were negligible when there was smooth contact or rotation around the pulley shafts. By leveraging the principle of geometric balance, this decoupling mechanism enhances the durability and stability of cable-driven systems without introducing complex structures. This approach can be extended to future applications involving multiple cables, such as cable-driven robotic arms, exoskeletons, robotic hands, continuum robots, and more.

Author Contributions: V.P.N.—concept, design, analysis, experiment, and writing, S.B.D.—experiment, analysis, writing, and proofreading. W.T.C.—concept and writing, funding acquisition, and revision. All authors have read and agreed to the published version of the manuscript.

Funding: This research is supported by the Schaeffler Hub for Advanced Research at NTU, under the ASTAR IAF-ICP Programme ICP1900093

Institutional Review Board Statement: Not applicable.

Informed Consent Statement: Not applicable.

Data Availability Statement: The data are contained within the article.

Conflicts of Interest: The authors declare no conflicts of interest.

References

1. Nikafrooz, N.; Leonessa, A. A Single-Actuated, Cable-Driven, and Self-Contained Robotic Hand Designed for Adaptive Grasps. *Robotics* **2021**, *10*, 109. [CrossRef]
2. Nguyen, V.P.; Dhyan, S.B.; Han, B.S.; Chow, W.T. Universally Grasping Objects with Granular—Tendon Finger: Principle and Design. *Micromachines* **2023**, *14*, 1471. [CrossRef] [PubMed]
3. Manti, M.; Hassan, T.; Passetti, G.; D'Elia, N.; Laschi, C.; Cianchetti, M. A Bioinspired Soft Robotic Gripper for Adaptable and Effective Grasping. *Soft Robot.* **2015**, *2*, 107–116. [CrossRef]

4. Goh, G.L.; Goh, G.D.; Toh, W.; Lee, S.; Li, X.; Lim, J.Y.; Li, Z.; Sinha, A.K.; Yeong, W.Y.; Campolo, D.; et al. A 3D Printing-Enabled Artificially Innervated Smart Soft Gripper with Variable Joint Stiffness. *Adv. Mater. Technol.* **2023**, *8*, 2301426. [CrossRef]
5. Goh, G.L.; Huang, X.; Toh, W.; Li, Z.; Lee, S.; Yeong, W.Y.; Han, B.S.; Ng, T.Y. Joint angle prediction for a cable-driven gripper with variable joint stiffness through numerical modeling and machine learning. *Int. J. Mater. Des.* **2024**, *1*, 62–74. [CrossRef]
6. Goh, G.D.; Goh, G.L.; Lyu, Z.; Ariffin, M.Z.; Yeong, W.Y.; Lum, G.Z.; Campolo, D.; Han, B.S.; Wong, H.Y.A. 3D Printing of Robotic Soft Grippers: Toward Smart Actuation and Sensing. *Adv. Mater. Technol.* **2022**, *7*, 2101672. [CrossRef]
7. Nguyen, V.P.; Dhyan, S.B.; Mai, V.; Han, B.S.; Chow, W.T. Bioinspiration and Biomimetic Art in Robotic Grippers. *Micromachines* **2023**, *14*, 1772. [CrossRef]
8. Van, N.P.; Anh, H.V. Grasping Interface With Wet Adhesion and Patterned Morphology: Case of Thin Shell. *IEEE Robot. Autom. Lett.* **2019**, *4*, 792–799.
9. Nguyen, V.P. Picking food by robot hand with tree-frog like pad in various wet conditions. *Eng. Res. Express* **2024**, *6*, 015086. [CrossRef]
10. Nguyen, P.V.; Sunil, D.B.; Chow, T.W. Soft-stable interface in grasping multiple objects by wiring-tension. *Sci. Rep.* **2023**, *13*, 21537. [CrossRef]
11. Nguyen, V.P.; Chow, W.T. Wiring-Claw Gripper for Soft-Stable Picking up Multiple Objects. *IEEE Robot. Autom. Lett.* **2023**, *8*, 3972–3979. [CrossRef]
12. Lin, J.; Chiang, C.K. Motion control of a cable-suspended robot using image recognition with coordinate transformation. *Proc. Inst. Mech. Eng. Part I J. Syst. Control Eng.* **2021**, *235*, 52–67. [CrossRef]
13. Tommasino, P.; Gamage, K.C.W.; Masia, L., Hughes, C.M.L.; Campolo, D. A novel robot for arm motor therapy with homogeneous mechanical properties. In Proceedings of the 2014 13th International Conference on Control, Automation, Robotics & Vision (ICARCV 2014), Singapore, 10–12 December 2014; Volume 6, pp. 1292–1297.
14. Campolo, D.; Tommasino, P.; Gamage, K.; Klein, J.; Hughes, C.M.; Masia, L. H-Man: A planar, H-shape cabled differential robotic manipulandum for experiments on human motor control. *J. Neurosci. Methods* **2014**, *235*, 285–297. [CrossRef] [PubMed]
15. Qian, S.t. A Review on Cable-driven Parallel Robots. *Chin. J. Mech. Eng.* **2018**, *31*, 66. [CrossRef]
16. Yeshmukhametov, A.; Koganezawa, K.; Yamamoto, Y. A Novel Discrete Wire-Driven Continuum Robot Arm with Passive Sliding Disc: Design, Kinematics and Passive Tension Control. *Robotics* **2019**, *8*, 51. [CrossRef]
17. Rao, P.; Peyron, Q.; Lilge, S.; Burgner-Kahrs, J. How to Model Tendon-Driven Continuum Robots and Benchmark Modelling Performance. *Front. Robot. AI* **2021**, *7*, 630245. [CrossRef]
18. Choi, K.; Kwon, J.; Lee, T.; Park, C.; Pyo, J.; Lee, C.; Lee, S.; Kim, I.; Seok, S.; Kim, Y.J.; et al. A hybrid dynamic model for the AMBIDEX tendon-driven manipulator. *Mechatronics* **2020**, *69*, 102398. [CrossRef]
19. Jiang, H.; Zhang, T.; Xiao, C.; Li, J.; Guan, Y. Modular Design of 7-DOF Cable-Driven Humanoid Arms. In *Proceedings of the Intelligent Robotics and Applications*; Yu, Y., Yu, J., Liu, L., Ju, Z., Liu, Y., Zhou, D., Eds.; Springer International Publishing: Cham, Switzerland, 2019.
20. Nguyen, V.P.; Chow, W.T.; Dhyan, S.B.; Zhang, B.; Han, B.S.; Wong, H.Y.A. Low-Cost Cable-Driven Robot Arm with Low-Inertia Movement and Long-Term Cable Durability. *Robotics* **2024**, *13*, 9.
21. Huang, L.; Liu, B.; Zhang, L.; Yin, L. Equilibrium Conformation of a Novel Cable-Driven Snake-Arm Robot under External Loads. *Micromachines* **2022**, *13*, 1149. [CrossRef]
22. Grosu, S.; De Rijcke, L.; Grosu, V.; Geeroms, J.; Vanderboght, B.; Lefeber, D.; Rodriguez-Guerrero, C. Driving Robotic Exoskeletons Using Cable-Based Transmissions: A Qualitative Analysis and Overview. *Appl. Mech. Rev.* **2019**, *70*, 060801. [CrossRef]
23. Sanjuan, J.; Castillo, A.; Padilla, M.; Quintero, M.; Gutierrez, E.; Sampayo, I.; Hernandez, J.; Rahman, M. Cable driven exoskeleton for upper-limb rehabilitation: A design review. *Robot. Auton. Syst.* **2020**, *126*, 103445. [CrossRef]
24. Kuan, J.Y.; Pasch, K.A.; Herr, H.M. A High-Performance Cable-Drive Module for the Development of Wearable Devices. *IEEE ASME Trans. Mechatronics* **2018**, *23*, 1238–1248. [CrossRef]
25. Wang, W.; Yu, L.; Yang, J. Toward force detection of a cable-driven micromanipulator for a surgical robot based on disturbance observer. *Mech. Sci.* **2017**, *8*, 103445. [CrossRef]
26. Jiang, S.; Hua, D.; Wang, Y.; Ju, F.; Yin, L.; Chen, B. Design and modeling of motion-decoupling mechanism for cable-driven joints. *Adv. Mech. Eng.* **2018**, *10*, 1687814018777428. [CrossRef]
27. Kim, Y.J. Design of low inertia manipulator with high stiffness and strength using tension amplifying mechanisms. In Proceedings of the 2015 IEEE/RSJ International Conference on Intelligent Robots and Systems (IROS), Hamburg, Germany, 28 September–2 October 2015; pp. 5850–5856.
28. Quigley, M.; Asbeck, A.; Ng, A. A low-cost compliant 7-DOF robotic manipulator. In Proceedings of the 2011 IEEE International Conference on Robotics and Automation, Shanghai, China, 9–13 May 2011; pp. 6051–6058.
29. Treratanakulchai, S.; Rodriguez y Baena, F. A Passive Decoupling Mechanism for Misalignment Compensation in Master-Slave Teleoperation. *IEEE Trans. Med Robot. Bionics* **2021**, *3*, 285–288. [CrossRef]
30. Liu, T.; Hao, G. Design of a Cylindrical Compliant Linear Guide with Decoupling Parallelogram Mechanisms. *Micromachines* **2022**, *13*, 1275. [CrossRef]
31. Zhao, B.; Nelson, C.A. Decoupled Cable-Driven Grasper Design Based on Planetary Gear Theory. *J. Med. Devices* **2013**, *7*, 020918. [CrossRef]

32. Wang, D.; Wu, J.; Wang, L. Research on the error transfer characteristics of a 3-DOF parallel tool head. *Robot. Comput.-Integr. Manuf.* **2018**, *50*, 266–275. [CrossRef]
33. Wang, D.; Wu, J.; Wang, L.; Liu, Y. A Postprocessing Strategy of a 3-DOF Parallel Tool Head Based on Velocity Control and Coarse Interpolation. *IEEE Trans. Ind. Electron.* **2018**, *65*, 6333–6342.
34. Gupta, B.S.; Ajayi, J.O.; Kutsenko, M. Experimental methods for analyzing friction in textiles. In *Friction in Textile Materials*; Gupta, B., Ed.; Woodhead Publishing: Sawston, UK, 2008; pp. 174–221.
35. Kuhm, D.; Bueno, M.A.; Knittel, D. Fabric friction behavior: Study using capstan equation and introduction into a fabric transport simulator. *Text. Res. J.* **2014**, *84*, 1070–1083. [CrossRef]
36. Yang, G.; Mustafa, S.K.; Yeo, S.H.; Lin, W.; Lim, W.B. Kinematic design of an anthropomimetic 7-DOF cable-driven robotic arm. *Front. Mech. Eng.* **2011**, *6*, 45–60.
37. Min, S.; Yi, S. Development of Cable-driven Anthropomorphic Robot Hand. *IEEE Robot. Autom. Lett.* **2021**, *6*, 1176–1183. [CrossRef]
38. Shi, K.; Song, A.; Li, Y.; Li, H.; Chen, D.; Zhu, L. A Cable-Driven Three-DOF Wrist Rehabilitation Exoskeleton With Improved Performance. *Front. Neurorobotics* **2021**, *15*, 664062. [CrossRef] [PubMed]
39. Ramirez, J.; Rubiano, A.; Castiblanco, P. Soft Driving Epicyclical Mechanism for Robotic Finger. *Actuators* **2019**, *8*, 58. [CrossRef]
40. Wang, Y.; Tian, Y.; She, H.; Jiang, Y.; Yokoi, H.; Liu, Y. Design of an Effective Prosthetic Hand System for Adaptive Grasping with the Control of Myoelectric Pattern Recognition Approach. *Micromachines* **2022**, *13*, 219. [CrossRef]
41. Nguyen, V.P.; Sunil Bohra, D.; Han, B.S.; Chow, W.T. Towards Flexible Manipulation with Wiring-Base Robot Hand. In *Proceedings of the Robot Intelligence Technology and Applications 7*; Springer: Cham, Switzerland, 2023; pp. 385–392.
42. Zhang, Y.; Xia, D.; Lu, Q.; Zhang, Q.; Wei, H.; Chen, W. Design, Analysis and Experimental Research of Dual-Tendon-Driven Underactuated Gripper. *Machines* **2022**, *10*, 761. [CrossRef]